High-speed transport-of-intensity phase microscopy with an electrically tunable lens

Chao Zuo,[1,2,3,*] Qian Chen,[1,3,5] Weijuan Qu,[4] and Anand Asundi[2]

[1]*Jiangsu Key Laboratory of Spectral Imaging & Intelligence Sense, Nanjing University of Science and Technology, Nanjing, Jiangsu Province 210094, China*

[2]*Centre for Optical and Laser Engineering, School of Mechanical and Aerospace Engineering, Nanyang Technological University, Singapore 639798, Singapore*

[3]*Key Laboratory of Photoelectronic Imaging Technology and System, Ministry of Education of China, Beijing Institute of Technology, Beijing 100081, China*

[4]*Centre for Applied Photonics and Laser Technology, Ngee Ann Polytechnic, 535 Clementi Road, 599489 Singapore*

[5]*chenq@njust.edu.cn*

[*]*surpasszuo@163.com*

Abstract: We present a high-speed transport-of-intensity equation (TIE) quantitative phase microscopy technique, named TL-TIE, by combining an electrically tunable lens with a conventional transmission microscope. This permits the specimen at different focus position to be imaged in rapid succession, with constant magnification and no physically moving parts. The simplified image stack collection significantly reduces the acquisition time, allows for the diffraction-limited through-focus intensity stack collection at 15 frames per second, making dynamic TIE phase imaging possible. The technique is demonstrated by profiling of microlens array using optimal frequency selection scheme, and time-lapse imaging of live breast cancer cells by inversion the defocused phase optical transfer function to correct the phase blurring in traditional TIE. Experimental results illustrate its outstanding capability of the technique for quantitative phase imaging, through a simple, non-interferometric, high-speed, high-resolution, and unwrapping-free approach with prosperous applications in micro-optics, life sciences and bio-photonics.

©2013 Optical Society of America

OCIS codes: (100.5070) Phase retrieval; (110.0180) Microscopy; (100.3010) Image reconstruction techniques; (120.5050) Phase measurement.

References and links

1. F. Zernike, "How I Discovered Phase Contrast," Science **121**(3141), 345–349 (1955).
2. G. Nomarski, "Differential microinterferometer with polarized waves," J. Phys. Radium **16**, 9s–13s (1955).
3. E. Cuche, P. Marquet, and C. Depeursinge, "Simultaneous amplitude-contrast and quantitative phase-contrast microscopy by numerical reconstruction of Fresnel off-axis holograms," Appl. Opt. **38**(34), 6994–7001 (1999).
4. U. Schnars and P. O. J. Werner, "Digital recording and numerical reconstruction of holograms," Meas. Sci. Technol. **13**(9), R85–R101 (2002).
5. B. Bhaduri, H. Pham, M. Mir, and G. Popescu, "Diffraction phase microscopy with white light," Opt. Lett. **37**(6), 1094–1096 (2012).
6. Z. Wang, L. Millet, M. Mir, H. Ding, S. Unarunotai, J. Rogers, M. U. Gillette, and G. Popescu, "Spatial light interference microscopy (SLIM)," Opt. Express **19**(2), 1016–1026 (2011).
7. B. Bhaduri, K. Tangella, and G. Popescu, "Fourier phase microscopy with white light," Biomed. Opt. Express **4**(8), 1434–1441 (2013).
8. M. Reed Teague, "Deterministic phase retrieval: a Green's function solution," J. Opt. Soc. Am. **73**(11), 1434–1441 (1983).
9. A. Barty, K. A. Nugent, D. Paganin, and A. Roberts, "Quantitative optical phase microscopy," Opt. Lett. **23**(11), 817–819 (1998).
10. D. Paganin and K. A. Nugent, "Noninterferometric Phase Imaging with Partially Coherent Light," Phys. Rev. Lett. **80**(12), 2586–2589 (1998).
11. L. Waller, Y. Luo, S. Y. Yang, and G. Barbastathis, "Transport of intensity phase imaging in a volume holographic microscope," Opt. Lett. **35**(17), 2961–2963 (2010).

#193903 - $15.00 USD Received 15 Jul 2013; revised 16 Sep 2013; accepted 17 Sep 2013; published 1 Oct 2013

12. L. Waller, S. S. Kou, C. J. R. Sheppard, and G. Barbastathis, "Phase from chromatic aberrations," Opt. Express **18**(22), 22817–22825 (2010).
13. P. F. Almoro, L. Waller, M. Agour, C. Falldorf, G. Pedrini, W. Osten, and S. G. Hanson, "Enhanced deterministic phase retrieval using a partially developed speckle field," Opt. Lett. **37**(11), 2088–2090 (2012).
14. S. S. Gorthi and E. Schonbrun, "Phase imaging flow cytometry using a focus-stack collecting microscope," Opt. Lett. **37**(4), 707–709 (2012).
15. M. Soto and E. Acosta, "Improved phase imaging from intensity measurements in multiple planes," Appl. Opt. **46**(33), 7978–7981 (2007).
16. L. Waller, L. Tian, and G. Barbastathis, "Transport of intensity phase-amplitude imaging with higher order intensity derivatives," Opt. Express **18**(12), 12552–12561 (2010).
17. C. Zuo, Q. Chen, Y. Yu, and A. Asundi, "Transport-of-intensity phase imaging using Savitzky-Golay differentiation filter--theory and applications," Opt. Express **21**(5), 5346–5362 (2013).
18. E. D. Barone-Nugent, A. Barty, and K. A. Nugent, "Quantitative phase-amplitude microscopy I: optical microscopy," J. Microsc. **206**(3), 194–203 (2002).
19. C. J. R. Sheppard, "Defocused transfer function for a partially coherent microscope and application to phase retrieval," J. Opt. Soc. Am. A **21**(5), 828–831 (2004).
20. L. Camacho, V. Micó, Z. Zalevsky, and J. García, "Quantitative phase microscopy using defocusing by means of a spatial light modulator," Opt. Express **18**(7), 6755–6766 (2010).
21. J. W. Goodman, *Introduction To Fourier Optics,* 3th ed. (Roberts & Company Publishers, 2005).
22. C. Falldorf, M. Agour, C. v Kopylow, and R. B. Bergmann, "Phase retrieval by means of a spatial light modulator in the Fourier domain of an imaging system," Appl. Opt. **49**(10), 1826–1830 (2010).
23. E. Hecht, *Optics,* 4th ed. (Addison-Wesley Longman, Incorporated, 2002).
24. L. J. Allen and M. P. Oxley, "Phase retrieval from series of images obtained by defocus variation," Opt. Commun. **199**(1-4), 65–75 (2001).
25. T. E. Gureyev and K. A. Nugent, "Rapid quantitative phase imaging using the transport of intensity equation," Opt. Commun. **133**(1-6), 339–346 (1997).
26. M. Beleggia, M. A. Schofield, V. V. Volkov, and Y. Zhu, "On the transport of intensity technique for phase retrieval," Ultramicroscopy **102**(1), 37–49 (2004).
27. D. Paganin, A. Barty, P. J. McMahon, and K. A. Nugent, "Quantitative phase-amplitude microscopy. III. The effects of noise," J. Microsc. **214**(1), 51–61 (2004).
28. K. Ishizuka and B. Allman, "Phase measurement of atomic resolution image using transport of intensity equation," J. Electron Microsc. (Tokyo) **54**(3), 191–197 (2005).
29. R. Bie, X.-H. Yuan, M. Zhao, and L. Zhang, "Method for estimating the axial intensity derivative in the TIE with higher order intensity derivatives and noise suppression," Opt. Express **20**(7), 8186–8191 (2012).
30. B. Xue, S. Zheng, L. Cui, X. Bai, and F. Zhou, "Transport of intensity phase imaging from multiple intensities measured in unequally-spaced planes," Opt. Express **19**(21), 20244–20250 (2011).
31. S. Zheng, B. Xue, W. Xue, X. Bai, and F. Zhou, "Transport of intensity phase imaging from multiple noisy intensities measured in unequally-spaced planes," Opt. Express **20**(2), 972–985 (2012).
32. C. J. Bellair, C. L. Curl, B. E. Allman, P. J. Harris, A. Roberts, L. M. D. Delbridge, and K. A. Nugent, "Quantitative phase amplitude microscopy IV: imaging thick specimens," J. Microsc. **214**(1), 62–69 (2004).
33. N. Streibl, "Three-dimensional imaging by a microscope," J. Opt. Soc. Am. A **2**(2), 121–127 (1985).
34. S. S. Kou, L. Waller, G. Barbastathis, P. Marquet, C. Depeursinge, and C. J. R. Sheppard, "Quantitative phase restoration by direct inversion using the optical transfer function," Opt. Lett. **36**(14), 2671–2673 (2011).
35. C. J. R. Sheppard, "Three-Dimensional Phase Imaging with the Intensity Transport Equation," Appl. Opt. **41**(28), 5951–5955 (2002).
36. V. V. Volkov, Y. Zhu, and M. De Graef, "A new symmetrized solution for phase retrieval using the transport of intensity equation," Micron **33**(5), 411–416 (2002).
37. W. Qu, C. O. Choo, V. R. Singh, Y. Yingjie, and A. Asundi, "Quasi-physical phase compensation in digital holographic microscopy," J. Opt. Soc. Am. A **26**(9), 2005–2011 (2009).
38. T. Yamauchi, H. Iwai, M. Miwa, and Y. Yamashita, "Low-coherent quantitative phase microscope for nanometer-scale measurement of living cells morphology," Opt. Express **16**(16), 12227–12238 (2008).
39. J. P. Guigay, M. Langer, R. Boistel, and P. Cloetens, "Mixed transfer function and transport of intensity approach for phase retrieval in the Fresnel region," Opt. Lett. **32**(12), 1617–1619 (2007).
40. J. Luo, K. Ying, P. He, and J. Bai, "Properties of Savitzky–Golay digital differentiators," Digit. Signal Process. **15**(2), 122–136 (2005).

1. Introduction

Many objects of interest in material and life science research are phase objects. These objects are visualized well by techniques such as Zernike phase contrast [1] and differential interference contrast microscopy [2], but neither of these methods provide quantitative phase information, which makes data interpretation difficult. Quantifying the optical phase shifts provides analytical information about the sample structures that can be used further for quantitative studies. The most well-established method for obtaining quantitative phase is

#193903 - $15.00 USD Received 15 Jul 2013; revised 16 Sep 2013; accepted 17 Sep 2013; published 1 Oct 2013
(C) 2013 OSA

through interferometry, such as digital holography [3, 4]. However, in most cases this class of methods relies on coherent illumination, therefore, plagued with problems of speckle that prevent the formation of high quality images. Recently, some alternative common path geometries have been reported, which allow for self-interference using white light illumination by spatial decomposition of the object field into its scattered, and un-scattered components [5–7]. These white-light methods eliminate the coherence noise, thus greatly improved the spatial resolution of the measurement. However, one always needs to make a compromise between the halo effect and the size of the source, i.e. the condenser aperture, which directly relates to the illumination power and the image quality [7].

On a different note, quantitative phase imaging can be realized by transport-of-intensity equation (TIE) using only object field intensities at multiple axially displaced planes [8]. TIE phase imaging have been increasingly investigated during recent years due to its unique advantages over interferometric techniques [9, 10]: it is non-interferometric, works with partially coherent illumination, computationally simple, no need to phase unwrapping, and does not require a complicated optical system. Despite these evident merits and great improvements, TIE has still *not* gained so much attention and widespread applications as interferometric techniques in the field of quantitative phase microscopy. One important reason is TIE typically requires a series of images captured at different focal depths, which is usually realized by translating the camera or the object manually or mechanically. This not only complicates the image acquisition process, but also prolongs the measurement time, precluding real-time observation of dynamic process. Although recent reports using volume holography [11], chromatic aberrations [12], spatial light modulator [13], and flow cytometry [14] can avoid the mechanical motion in the intensity stack acquisition, a simple, practical, non-mechanically controlled focus-variable system that can deliver diffraction-limited imaging performance for dynamic TIE phase imaging is still quite demanding.

The goal of this paper is to introduce a tunable-lens based TIE phase microscopy system named TL-TIE, which takes full advantages of high-speed, high-resolution, high-sensitive, and low-cost. Specifically, we introduce an electronically tunable lens (ETL) with an additional 4*f* relay system to the camera port of a commercial inverted microscope, which allows for rapid electronically controlled re-focusing with constant magnification without affecting the original high imaging quality of the microscope. The simplified image stack collection significantly reduces the acquisition time, making dynamic TIE phase imaging possible. Loss of spatial resolution in TIE phase imaging is another common and but vexing problem which, in general, depends on the nonlinearity error in longitudinal intensity derivative estimation and the illumination condition of the object under investigation. The nonlinearity error can be corrected by using more intensity measurements at multiple planes [15–17] at the expense of prolonging the measurement time due to manual or mechanical adjustment of the measurement planes. With the TL-TIE system, it takes only about 2 seconds to record the 31 images intensity stack, and from which precise profiling of microlens array can be achieved by employing the optimal frequency selection [17] scheme in TIE. The dynamic phase imaging ability of TL-TIE is also demonstrated via monitoring live cells in culture medium. The phase blurring in traditional TIE is corrected by the deconvolution based on the defocused phase optical transfer function [18, 19], allowing high-resolution, dynamic TIE phase imaging with only three intensity recordings.

2. Experiential configuration and characterization

TIE imaging involves refocusing the imaging system in order to record a series of images at different focus distances through the object. We achieve this by adding an image relay system to the camera port of a commercial inverted microscope. The relay system consists of a standard 4*f* system with an ETL combined with a plane concave offset lens (OL) located at the Fourier plane. Figure 1 shows the experimental configuration, wherein a halogen white light source with a green interference filter (central wavelength $\lambda = 550$ nm, 45 nm

#193903 - $15.00 USD Received 15 Jul 2013; revised 16 Sep 2013; accepted 17 Sep 2013; published 1 Oct 2013
(C) 2013 OSA

bandwidth) is used for illumination. A commercial inverted bright field microscope (Olympus IX71), which itself is composed of a collector lens, condenser aperture diaphragm, condenser lens, objective, reflective mirror (M_1), and tube lens, produces a magnified image of the specimen at the camera port (image plane). All the objectives used are infinity-corrected and matched the focal length of the tube lens (180 mm). From the image plane of the microscope, two lenses L_1 and L_2 (focal length $f = f_1 = f_2 = 150$ mm) form a 4*f* system. The ETL we used is a plane convex one (EL-C-10-30-VIS-LD, Optotune AG, Switzerland), with tunable focal length range of + 50 to + 200 mm and 10 mm clear aperture. To realize refocusing along positive and negative directions with respect to the intermediate image plane, the ETL was paired with the plane concave OL (focal length −100 mm). The final images are captured by a monochrome CCD camera (The Imaging Source DMK 41AU02, 1280 × 960, 4.65 μm pixel size, 15 fps) .

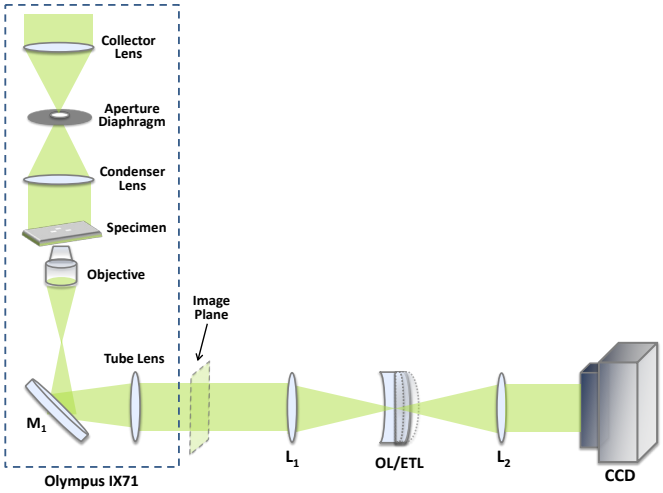

Fig. 1. Schematic setup for TL-TIE system. A 4*f* system with OL/ETL located at the Fourier plane is attached to Olympus IX71 bright field microscope. The Fourier lens L_1 relays the back focal plane of the objective onto the OL/ETL. Fourier lens L_2 reconstructs the final image at the CCD plane, which is conjugated with the image plane. The shift of the object plane with equal magnification can be realized adjusting the focal length of ETL.

2.1 Telecentricity

One important assumption inherent in TIE phase imaging is the system should be telecentric [18]. This assumption guarantees that the refocusing does not introduce phase curvature over the field of view so that the through-focus stack can deliver a series of images with equal magnification. In a non-telecentric system, the object to image distance changes for each plane imaged, with the result that the images of the different object layers are recorded with a different magnification [20]. The need to rescale the images of each layer only complicates the data processing, but also introduces the possibility of error. The telecentricity in the proposed system can be easily interpreted by physical optics, since it emulates the process of the angular spectrum propagation. From the angular spectrum perspective, the propagation of wavefield $u_0(x, y)$ from the focus plane to the parallel plane at nonzero distance Δz is described by [21]

$$u_{\Delta z}(x, y) = \mathscr{F}^{-1}\left\{\mathscr{F}\left\{u_0(x, y)\right\} H_{\Delta z}(u, v)\right\}, \tag{1}$$

Where $\mathscr{F}$ is the Fourier transform, (u, v) is the vector in frequency space corresponding to the transverse spatial coordinate (x, y) . The function H is the transfer function for free space, and in paraxial approximation it is given by

#193903 - $15.00 USD Received 15 Jul 2013; revised 16 Sep 2013; accepted 17 Sep 2013; published 1 Oct 2013
(C) 2013 OSA

$$H_{\Delta z}(u,v) = \exp\left[-i\pi\lambda\Delta z\left(u^2+v^2\right)\right], \tag{2}$$

Note here we neglect the constant phase factor $\exp(jkz)$, where k is the wave number. The discrete version of Eq. (2) is well known as angular spectrum method [4], which is widely used in digital holographic reconstruction. The major advantage of angular spectrum method is its ability to maintain the size of the image field, independent of the propagation distance Δz. Considering the Fourier transform property of the 4*f* system, the above described free-space propagation process can be physically emulated by modulating the light incident in the Fourier plane with the propagation transfer function using a phase SLM [13, 22]. However, some inherent limitations of SLM devices, such as relatively large pixels, less than 100% fill factor, high cost, restrict its performance and potential applications. Here we use a tunable lens in place of the SLM. With the paraxial approximation, the phase transformation of the combination of the ETL/OL can be represented by [21, 23],

$$t_l(\xi,\eta) = \exp\left[-\frac{i\pi}{\lambda f_c}\left(\xi^2+\eta^2\right)\right], \tag{3}$$

where

$$f_c = \frac{f_{ETL}f_{OL}}{f_{ETL}+f_{OL}-d}. \tag{4}$$

Here d is the axial distance between the two lenses, and (ξ,η) is the spatial coordinates in the Fourier plane of the 4*f* setup. Note here we consider the composite lens as 'thin' for simplicity, because d is very small (the distance from the plane surface of the OL to the ETL housing is 4 mm) and f_c is much larger than thickness of the two lenses. Comparing Eq. (3) with Eq. (2), we can see the $t_l(\xi,\eta)$ share the same format as the propagation transfer function. With use of the connection between the frequency coordinates in the Fourier domain (u,v) and the spatial coordinates in the Fourier plane of the 4*f* setup (ξ,η) [21], the relationship between the focal length variations versus the propagation distances can be established:

$$\Delta z = \frac{f^2}{f_c} = \frac{f^2\left(f_{ETL}+f_{OL}-d\right)}{f_{ETL}f_{OL}}. \tag{5}$$

Where f is the focal length of the two Fourier lenses L_1 and L_2 (f = 150 mm). Since f_{ETL} can be electronically controlled, the defocus distance Δz can be easily adjusted whilst maintaining the position of the infocus image plane and image magnification. Note the focal distance shift mentioned in the above derivation is with respect to the magnified object field at the image plane of the microscope camera port. The actual axial focus shift at the real object-plane at the sample stage can be obtained by $\Delta z/M^2$, where M is the magnification of the objective used.

2.2 Defocusing properties and accuracy

In our setup, the ETL was driven by a custom current source, which offered an adjustable full-scale output current from 0 to 300 mA, with a resolution up to 0.1 mA. Figure 2(a) shows the lens focal length tuning as a function of current, $f_{ETL}(I)$, measured by a beam diagnostics digital CMOS camera (LaserCam-HR, Coherent) with a collimated input beam. The overall trend of the curve is nonlinear but for the current range 120 mA to 180 mA (corresponding to the focal length range about 86 ~118 mm), the focal length varies almost linearly with current. With reference to Eq. (5), the range of Δz can be estimated to be about ± 30 mm within this current range, which is sufficient for our applications because TIE does not require a large

#193903 - $15.00 USD Received 15 Jul 2013; revised 16 Sep 2013; accepted 17 Sep 2013; published 1 Oct 2013
(C) 2013 OSA

defocus range. However, it is inappropriate to directly apply Eq. (5) to derive the current to focus-shift function for our system because it is only valid for ideal conditions when all lenses are considered as 'thin'. For this reason, we use the optical design software ZEMAX to model our system (from the image plane of the microscope to the CCD plane) in more realistic conditions. Figure 2(b) shows the curve of simulated focal length variations versus the focus shifts, and the one calculated using Eq. (5) with d = 4.5 mm (to best fit the simulation result). We also measured the real focus shifts of the system as a function of current by refocusing a 5 μm pinhole using the camera mounted on a motorized translation stage, as shown in Fig. 2(b). It was found that the measured data fitted the simulated curves well and deviated from the Eq. (5) about 3 mm when the current reaches 180 mA. The standard deviation between measurement and simulated curve was 0.275 mm and we found there was always a bias of 0.18 mm between the measured data and the simulated result. This discrepancy may be due to manufacturing errors, the errors arising from estimation of 'best focus', and most probably misalignment in the optics. Therefore, we shifted the simulated curve by 0.18 mm as our ideal current to focus-shift function, and in this case, the standard deviation between measurement and the shifted curve was reduced to 0.0971 mm (smaller than the quantitation error). The resolution of current control is 0.1 mA, so the minimum step controllable for the focus shift is about 130 μm, corresponding to 36.1 nm focus shift at the real object plane when a 60x objective is used, which is sufficient to ensure a high-precision measurement.

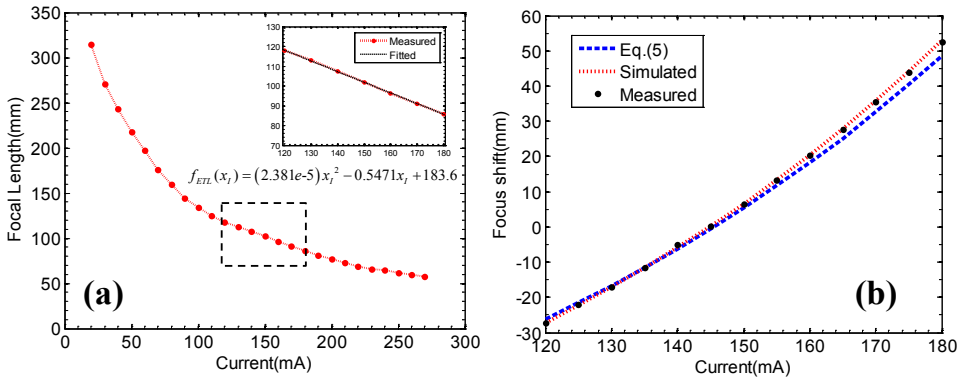

Fig. 2. Defocusing characterization of the tunable lens and the TL-TIE system. (a) Measured focal length calibration curve of the ETL as a function of current. The region in the dashed box (magnified in the inset) shows good linearity of response. (b) The theoretical [Eq. (5)], simulated, and measured focus-shift curves of the TL-TIE system.

2.3 Real system performance

It is well accepted that the commercial microscope from major companies could deliver diffraction-limited image quality. The TL-TIE is acted as an add-on module of a commercial microscope; it should be able to reproduce the diffraction-limited images to the CCD plane with fidelity. Since the additional 4*f*-relay system and the ETL/OL follows behind the image plane of the microscope and the numerical aperture (NA) at the image plane is quite limited ($NA_{\text{image}} \approx NA_{\text{obj}}/M$), it is not difficult to achieve diffraction-limited imaging performance for our TL-TIE system even with use the off-the-shelf optical components. The simulated spot diagram of the system is shown in Fig. 3(a), assuming the NA_{image} = 0.015 (the object is imaged by a 40x MO with 0.6NA). The blue, green, red, color stand for three fields with 0, 1.5 and 3 mm (approximately at the edge of the CCD plane) distance from the optics axis, showing that all the rays fall into the Airy disk circle. The RMS wavefront was simulated to be within $\lambda/150$ for the full field. Figure 3(b) shows the modulation transfer function (MTF) of the system, which is nearly coincident with the diffraction limit. The point spread function (PSF) of the whole system was also measured by using a 0.5 μm pinhole to approximate a

#193903 - $15.00 USD Received 15 Jul 2013; revised 16 Sep 2013; accepted 17 Sep 2013; published 1 Oct 2013
(C) 2013 OSA

point source with 40x plan semi-apochromat objective (Olympus, LUCPLFLN 40X, NA = 0.6). Figures 3(c) and 3(d) show the sharpest infocus images and their respective Gaussian fitted cross-sections of the raw microscope (without the ETL) and the TL-TIE system. The full width half maximum (FWHM) of the PSF is 1.13 μm for the raw microscope and 1.16 μm when our TL-TIE module was included. The telecentricity of the system was simulated to be within 0.0001 in the defocus range used and experimentally verified to be within 0.005 for the whole defocus range, indicating that the changes of image magnification with focus distance can be neglected. From the simulated and measured data, we may safely conclude that our modified TL-TIE system redelivers the high image quality of the original microscope and meanwhile with the telecentricity well preserved. It should be note that TIE as well as the TL-TIE system is inherently based on the paraxial assumption. However, whereas the microscope is a non-paraxial system, the wave-field at the image plane of an optical microscope can be considered paraxial due to the limited NA. Since TL-TIE system defocus the wavefield at the image plane and meanwhile TIE measure not exactly the object phase but the phase of the wavefield in the image plane, the paraxiality can be regarded as a reasonable assumption.

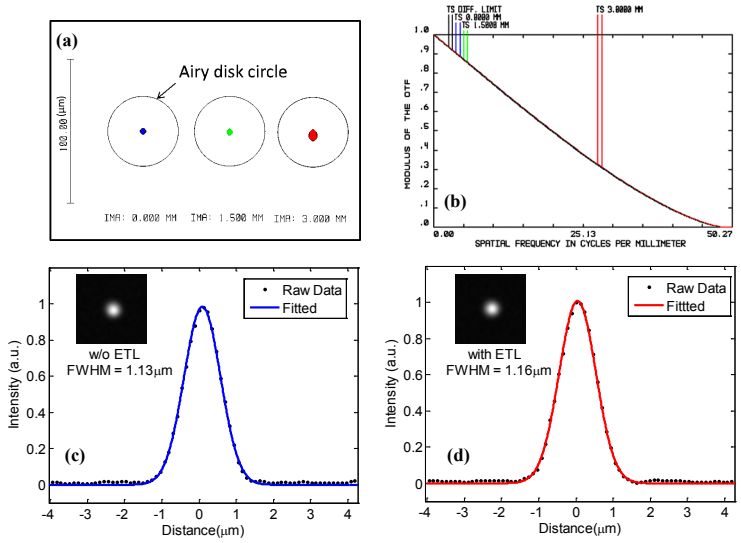

Fig. 3. Simulations and real performance of TL-TIE systems with a 40x objective (NA = 0.6). (a) Simulated spot diagrams. (b) Simulated MTF. (c) PSF measured using a 500 nm pinhole without the TL-TIE relay system. (d) Measured PSF of the whole TL-TIE system. The cross-sectional slices are fitted by the Gaussian function.

2.4 Speed

With the help of ETL, intensity images at different distances can be rapidly acquired by the CCD camera through electrical control without any mechanical motion. The response time of the ETL used was 15 ms, which enables time division multiplexing scanning with fast switching rate. We use a self-developed Field-Programmable Gate Array (FPGA) board to control the SPI signal with the current source and generate the trigger pulses for the camera to properly synchronize it with the ETL. Currently, the speed of our system is limited by the camera with maximum acquisition speed of 15 frame/s, thus the maximum rate of the phase reconstruction is 5 frame/s (using 3 intensity images for each reconstruction). We also developed a software using Microsoft Visual Studio 2008 with C++, with which the phase imaging can be realized in real-time and all raw images can be saved as a video sequence for post-processing. For static object measurement, we can also use more intensity images for phase extraction to improve accuracy without worrying about the motion-induced error. The

#193903 - $15.00 USD Received 15 Jul 2013; revised 16 Sep 2013; accepted 17 Sep 2013; published 1 Oct 2013
(C) 2013 OSA

related numerical processing algorithms will be introduced in details in Section 3. It should be note that since the maximum refresh rate for ETL is about 67 images/s in principle, the imaging speed could be increased to video rate by employing a camera with higher speed and sensitivity.

3. Numerical processing

The numerical processing involved in the current method is based on TIE, which outlines the object-plane phase to the first derivative of intensity with respect to the optical axis in the near Fresnel region [8]:

$$-k\frac{\partial I(\mathbf{r})}{\partial z}=\nabla\cdot\left[I(\mathbf{r})\nabla\phi(\mathbf{r})\right], \tag{6}$$

where $\mathbf{r}$ is the position vector representing the transverse spatial coordinates (x,y). ∇ is the gradient operator over the transverse direction $\mathbf{r}$. z denotes the optics axis, perpendicular to the x,y plane. I is the infocus image intensity ($I=I_0=|u_0|^2$). To solve TIE, usually an auxiliary function ψ satisfying $\nabla\psi=I\nabla\phi$ is introduced [8, 24], and thus TIE is converted to the following two Poisson equations

$$-k\frac{\partial I}{\partial z}=\nabla^2\psi, \tag{7}$$

and

$$\nabla\cdot\left(I^{-1}\nabla\psi\right)=\nabla^2\phi. \tag{8}$$

The second Poisson equation [Eq. (8)] is used for phase integration from $\nabla\phi=I^{-1}\nabla\psi$. For pure phase object, I is assumed to be constant and then TIE can be reduced to only one Poisson equation:

$$-\frac{k}{I}\frac{\partial I}{\partial z}=\nabla^2\phi, \tag{9}$$

The Poisson equations can be easily solved with fast-Fourier transform (FFT) [10, 25] for speedy processing of the inverse Laplacian, thus the phase ϕ can be uniquely determined with the intensity I and longitude intensity derivative $\partial I/\partial z$. Experimentally, I is easy to obtain. However, the intensity derivative along the optic axis cannot be directly measured. Conventionally, it is approximated by a finite difference between two out-of-focus images, recorded symmetrically about the in-focus plane with $\pm\Delta z$ defocus distance [26–28].

$$\frac{\partial I(\mathbf{r})}{\partial z}\approx\frac{I_{\Delta z}(\mathbf{r})-I_{-\Delta z}(\mathbf{r})}{2\Delta z}. \tag{10}$$

Mathematically, this approximation is valid in the limit of small defocus distances, but experimentally, the derivative estimate will become quite unstable when the distance Δz is too small because of the noise and quantitation error [16, 17]. On the other hand, increasing the two-plane separation Δz provides better signal-to-noise ratio (SNR) in the derivative estimate; however, the breakdown of the linear approximation induces nonlinearity errors, which results in the loss of the phase lateral resolution.

3.1 Numerical algorithm for static object measurement - Optimal Frequency Selection

For static object measurement, we can simply increase the number intensity measurements at multiple planes [15, 16, 29–31] to account for both phase SNR and nonlinearity error. The detailed algorithm is based on the optimal frequency selection (OFS) scheme described in

#193903 - $15.00 USD Received 15 Jul 2013; revised 16 Sep 2013; accepted 17 Sep 2013; published 1 Oct 2013
(C) 2013 OSA

[17]. With more intensity measurements $I_{j\Delta z}(\mathbf{r}), j=-n,...,0,...,n$, the longitudinal intensity derivative can be represented by their linear combination:

$$\frac{\partial I(\mathbf{r})}{\partial z} \approx \sum_{j=-n}^{n} \frac{a_j I_{j\Delta z}(\mathbf{r})}{\Delta z}. \tag{11}$$

Thus, it offers more flexibility for improving the accuracy and noise resistance in derivative estimation. The only difference in these multiple planes derivative estimation methods [15, 16, 29–31] lies in the coefficients a_i in Eq. (11), and it has been found that all these method can be unified into Savitzky-Golay differentiation filter (SGDF) with different degrees if the finite difference [Eq. (11)] is viewed from the viewpoint of the digital filter [17]. The OFS is a three-step process with the basic idea that selecting the optimal components of the phase recovered from SGDFs with various degrees in spatial frequency domain: First, estimate the intensity derivatives with SGDFs with different degrees through Eq. (11). Second, reconstruct the phase distributions with TIE by solving the two Poisson equations [Eqs. (7) and (8)] with the estimated intensity derivatives. Finally, extract the optimal frequency components from these phase distributions using a complementary filter bank in spatial frequency domain and then recombine them into a composite phase. In [17], the OFS is derived based on first-order Born (weak scattering) approximation, which in turn requires that the amplitude and phase modulation of the object are small. However, as we shown in Appendix I, the first-order Born approximation is actually unnecessary and the OFS can be validated making only the assumption of slowly-varying object. Thus, it can be well applied to different types of objects even their phase modulations are not weak. It also should be note that mathematical derivation of OFS method assumes that the optical field is spatially coherent and thus it is required to constrict the condenser aperture to increase the spatial coherence of the illumination.

3.2 Numerical algorithm for dynamic measurement- inversion of defocused phase OTF

For dynamic measurement, using the minimum intensity measurements is preferable and thus the intensity derivative is estimated by Eq. (10) with two intensity measurements. In this case, a slightly larger defocus distance is used to increase SNR in derivative estimate. The spatial coherence of the illumination, which is quantified by the *coherence parameter* - the ratio of condenser to objective numerical apertures ($S = NA_{cond} / NA_{obj}$) is increased to 0.3~0.4 to ensure certain degree of spatial coherence and enough illumination power. The loss of spatial resolution of the phase reconstructed by TIE is closely related to the defocus distance and coherent parameter, and more detailed investigations on their relations can be found in [18, 32]. Instead of directly solving the TIE [Eq. (6)], we make use of the concept of defocused phase optical transfer function (OTF) that accounts for phase blurring due to the nonlinearity error and effect of the partially coherent illumination. The root of the loss of spatial resolution in TIE phase retrieval can be more clearly identified if we take Eq. (10) into Eq. (7) and then transform the result into Fourier domain:

$$\frac{\hat{I}_{\Delta z}(\mathbf{u}) - \hat{I}_{-\Delta z}(\mathbf{u})}{4} = \pi \Delta z \lambda u^2 \hat{\psi}(\mathbf{u}). \tag{12}$$

Here $\mathbf{u}$ is the Fourier domain coordinates corresponding to $\mathbf{r}$. For pure-phase objects (e.g. biological tissues and cells) $I \approx \text{constant}$, we can also obtain the similar result by taking Eq. (10) into Eq. (9). Therefore the phase contrast transfer function (CTF) implied in traditional TIE has the form

$$T_{TIE}(\mathbf{u}) = \pi \Delta z \lambda u^2. \tag{13}$$

#193903 - $15.00 USD Received 15 Jul 2013; revised 16 Sep 2013; accepted 17 Sep 2013; published 1 Oct 2013
(C) 2013 OSA

The solution of the Poisson equation Eq. (7) can be interpreted by an inverse filtering process in frequency domain with the filter response $T_{TIE}^{-1}(\mathbf{u})$. It can be seen that the underlying assumption in TIE is the phase contrast increases linearly with defocus distance and quadratically with spatial frequencies. This assumption is obviously unreasonable since the phase contrast cannot arbitrarily increase with defocus distance or spatial frequencies. The overestimate of the phase contrast in high-spatial frequency domain is the primary cause of phase blurring if one uses TIE improperly beyond the small-defocus regime. The three-dimensional optical transfer function theory described by Streibl [33] is an accurate and comprehensive model to analyze image formation for weakly scattering object under partially coherent illumination in a bright-field microscope. Based on this theory, the weak defocus phase OTF can be derived [18, 19], which has been already used for analyzing [18, 32] and improving [34] the performance of TIE under partially coherent illumination. By using Fourier slice theorem, and after some algebra similar to that of [18], we can obtain the defocus phase OTF (DPOTF)

$$T_p(\mathbf{u}) = \frac{1}{2}\int T_p^{(3)}(\mathbf{u},\eta)\sin(2\pi\Delta z\eta)\,d\eta. \tag{14}$$

where η is the spatial frequency in the longitudinal direction. $T_p^{(3)}(\mathbf{u},\eta)$ is the normalized three-dimensional phase transfer functions for a bright-field microscope with circular objective and condenser aperture [33, 35]. Note Eq. (14) is valid beyond the limit of small distances since we do not impose the weak defocus assumption as in [34]. Therefore, we can use the DPOTF [Eq. (14)] to replace the phase CTF of TIE [Eq. (13)] to correct the phase blurring related to the defocus distance and partially coherence of the illumination. So instead of solving the Poisson equation Eq. (7) [or Eq. (9) for pure phase object] by inverse Laplacian with the filter response $T_{TIE}^{-1}(\mathbf{u})$, we perform a deconvolution based on $T_p^{-1}(\mathbf{u})$ with an ad hoc Tikhonov regularization to solve for ψ (or direct obtain for ϕ pure phase object). This method here is called inversion of defocused phase optical transfer function (IDPOTF). Note the DPOTF in Eq. (14) cannot be expressed analytically, so numerical calculation methods are required for computing the integral on the right hand side.

4. Experimental results

4. 1 Characterization of microlens array using OFS

As the first experiment, a plano-convex microlens array with 30 μm pitch from SUSS MicroOptics was used as the test sample. The sample is imaged with a 40x microscope objective (Olympus, LUCPLFLN 40X, NA = 0.6) and the condenser aperture diaphragm was stopped down to only 15% of the objective NA ($NA_{cond} = 0.09$) so that the illumination is close to spatially coherent. Since the object is static, the OFS method described in Sec. 3.1 was used for phase reconstruction. The defocus distance was controlled from −15μm to 15μm in steps of 1 μm at a switching rate of 15 Hz, and the image stack was captured within two seconds with the TL-TIE system.

The acquired video of the intensity image stack is shown in Media 1, and some selected intensity images at different defocus distances are shown in Figs. 4(a)–4(e). The phase reconstructed from OFS is shown in Fig. 4(f). Note the FFT-based Poisson Solver [25] implies periodic boundary conditions (BC) [36]. To prevent the phase artifacts due to improper BC, we used a mask to exclude the microlens located around the edge of the images, assuming the phase is flat at the image boundary, so that the periodic boundary conditions can be fulfilled by the modified experimental data. Then only the central portion [indicated by the white dot box in Fig. 4(c)] was extracted for further analysis. The corresponding three-dimensional (3D) profile is shown by converting the phase to the physical height of the lens [the refractive index of lens material (fused silica) is 1.46]. For comparison, the same sample was also measured using a digital holographic microscopy (DHM) system (laser wavelength

#193903 - $15.00 USD Received 15 Jul 2013; revised 16 Sep 2013; accepted 17 Sep 2013; published 1 Oct 2013
(C) 2013 OSA

650 nm, magnification 43x), described in detail in [37]. Figure 4(g) shows the digital hologram captured and the high-frequency carrier fringes due to the off-axis geometry are clearly visible in the enlarged area. Its numerically reconstructed phase is shown in Fig. 4(h). To quantify the measurements accuracy, we show one cross-section from each result, labeled by the red and blue dashed lines in Figs. 4(f) and 4(h), respectively. It can be seen the height distribution obtained using OFS with TL-TIE system is in good agreement with the DHM measurement. The calculated radius of curvature (ROC) is 399 μm for OFS and 382 μm for DHM, both correspond reasonably well to the ROC value provided by the supplier (390 μm).

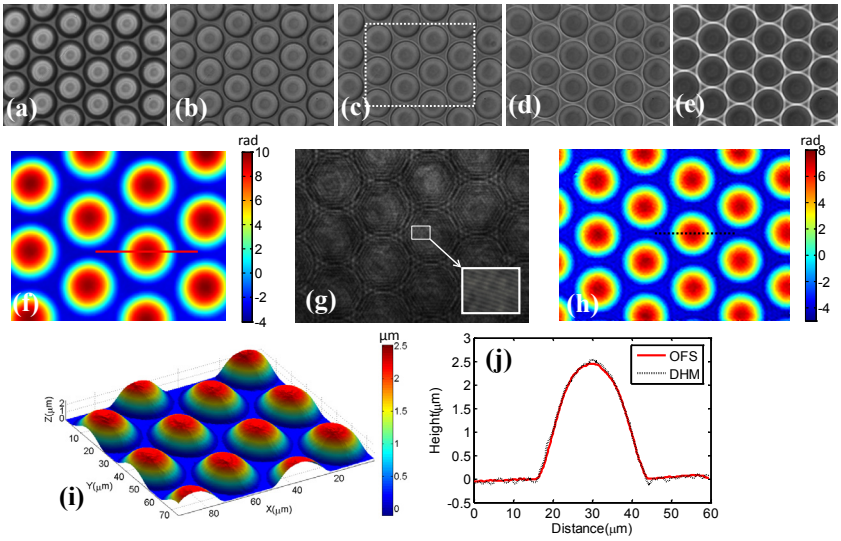

Fig. 4. (Media 1) Microlens array characterization using OFS. (a-e) Recorded intensity images with defocus distance 15, 5, 0, −5, −15 μm, respectively. (f) Quantitative phase recovered by OFS. (g) Digital hologram captured by a DHM system. The carrier fringes can be easily seen in the magnified area. (h) Unwrapped phase of DHM. (i) 3D rendering of the OFS result. (j) Line profiles corresponding to the red solid line in (f) and the black dotted line in (h), respectively.

The intensity stack shown in Media 1 was captured with 50 ms exposure time, which ensures a relatively high image quality. However, for some particular applications where the exposure time is limited or/and the intensity signal is relative weak, noise may be comparable with the signal. To simulate this environment, the captured intensity data was further artificially corrupted by simulated Gaussian white noise, giving the peak signal-to-noise ratio (PSNR) about −2. To clearly demonstrate the noise level. three corrupted intensity images are shown in Figs. 5(a-c), respectively. Since TIE can only determine the phase uniquely up to an additive constant, the mean values of each result were adjusted to same level for better comparisons. In this case, the traditional TIE with 2-plane separation of ±1 μm gave a noisy result with low-frequency artifacts, which deformed the basic structure of the lens phase [Fig. 5(d)]. The phase SNR was improved by using the 9th-order TIE [9th-degree SGDF, as shown in Fig. 5(e)]. However, the result demonstrated the high-order TIE is still very sensitive to noise. Under severely noisy conditions, 1st-order TIE (1st-degree SGDF) was used for its best noise resistance (with lowest noise reduction factor) and the SNR and the contrast of the recovered phase greatly improved, as shown in Fig. 5(f). The phase recovered using OFS [Fig. 5(g)] is rather similar with that of 1st-degree SGDF at the first glance. However, closer inspection along one cross-section [Fig. 5(h)] revealed that the 1st-degree SGDF distorted the over-smooth the phase due to the nonlinearity error while OFS method reliably followed the sudden phase turning, as shown in Fig. 5(i). The experimental results further demonstrate the robustness of the OFS method under noisy conditions.

#193903 - $15.00 USD Received 15 Jul 2013; revised 16 Sep 2013; accepted 17 Sep 2013; published 1 Oct 2013
(C) 2013 OSA

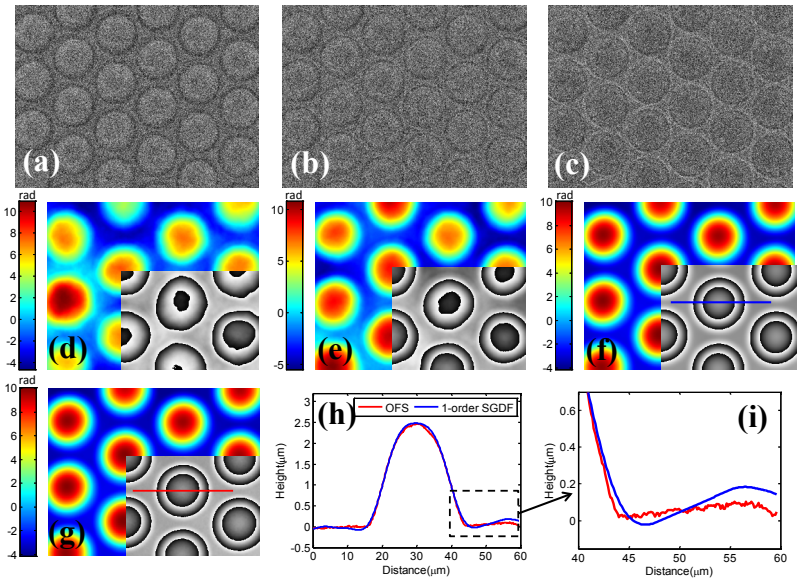

Fig. 5. Phase retrieval comparison under severely noisy conditions. (a-c) Intensity images with defocus distance 5, 0, −5μm after adding artificial noise. (d) Phase recovered by traditional TIE with 2-plane separation of ± 1μm. (e) Phase recovered by 9th-order TIE (9th-degree SGDF). (f) Phase recovered by 1st-order TIE (1st-degree SGDF). (g) Phase recovered by OFS. The lower-right portion of each image shows the corresponding digitally rewrapped phase within range $[-\pi, \pi)$. (h) The cross-sectional profiles corresponding to the blue and red lines in (f) and (g), respectively. (i) The magnified area corresponding to the boxed region in (e).

4.2 Dynamic phase imaging of live cells by IDPOTF

Next we demonstrate using the TL-TIE system to monitor unstained live breast cancer cells (MCF-7) cultured in Dulbecco's Modification of Eagle's Medium supplemented with 10% fetal bovine serum. For dynamic measurement, the IDPOTF method described in Sec. 3.2 was used for phase reconstruction. In this experiment, the specimens was imaged used a 60x plan semi-apochromat objective (Olympus, LUCPLFLN 60X, NA = 0.7), and the coherence parameter S was adjusted to 0.35. The phase imaging operated at 2 frames/s as the camera was running at acquisition rate of 6 frames/s to ensure sufficient exposure time and good image quality.

Figures 6(a)–6(c) show three recorded images corresponding to focus distance –2.5, 0, and + 2.5 μm, respectively, from which the quantitative phase image can be recovered by either the traditional TIE [Fig. 6(d)] or IDPOTF [Fig. 6(e)]. Enlarged images of the parts identified by the red squares are shown in the insets of Figs. 6(d) and 6(e). It can be seen the IDPOTF recovered the details of the fine structure of the specimen, which are hard to be observed in the traditional TIE result. To investigate the resolution increase obtained by IDPOTF, the phase CTF of TIE calculated from Eq. (13) and the DPOTF calculated from Eq. (14) using the system parameters of the current experimental are plotted respectively in Fig. 6(f). It is apparent that the two curves start to deviate at spatial frequencies > 0.3 μm^{-1} because the TIE is based on the assumption of perfect imaging and wrongly assumes that the phase contrast is increased quadratically with spatial frequency, which is not fulfilled in a real microscope. It can also be predicted that the TIE cannot retrieve the phase structure with spatial frequencies above 0.5 μm^{-1} due to the significant discrepancy between the TIE phase CTF and the DPOTF. However, the maximal theoretical phase resolution achieved by IDPOTF is about 0.8 μm^{-1} which corresponds to first zero-crossing of the DPOTF curve [the actual value should be larger because only the frequency falls in the vicinity of 0.8 μm^{-1} is unrecoverable, and some higher frequency components still shows (inverse) phase contrast],

#193903 - $15.00 USD Received 15 Jul 2013; revised 16 Sep 2013; accepted 17 Sep 2013; published 1 Oct 2013
(C) 2013 OSA

corresponding to 60% increase in resolution compared with traditional TIE method. To further confirm the increase in resolution in real images, we examined two point-like tiny features approximately 1.6 μm apart (corresponding to the spatial frequency 0.625 μm^{-1}) from the magnified regions of Figs. 6(d) and 6(e). It can be seen from the two cross-sections shown in Fig. 6(g), the structures are clearly distinguished by the IDPOTF method, while cannot resolved in the traditional TIE result, which is in agreement with our theoretical analysis.

Before proceeding any further, the following points should be clarified: First, the IDPOTF method could improve the phase resolution compared with traditional TIE, but it is still subject to the diffraction limit of the imaging system because insofar we are extracting phase information from the measured intensity images. Second, the improvement of the resolution is not fixed, but dependent on the system parameters, i.e., the coherence parameter and the defocus distance, which determine the coincidence degree between the TIE phase CTF and the DPOTF. Third, reducing the defocus distance (e.g. to 0.5 μm) improve the theoretical phase resolution and meanwhile reduce the SNR of the reconstructed phase of IDPOTF (as can be seen from Fig. 6(f) the DPOTF curve assume larger values at higher frequencies and smaller values at lower spatial frequencies compared with the case when Δz = 2.5 μm). Finally, the use of the IDPOTF method instead of TIE merely improves the phase spatial resolution without affecting the accuracy of quantitative phase measurement (mostly characterized by low spatial frequency phase components) because the DPOTF always converges to the CTF of TIE [Eq. (17)] with the decrease in spatial frequencies.

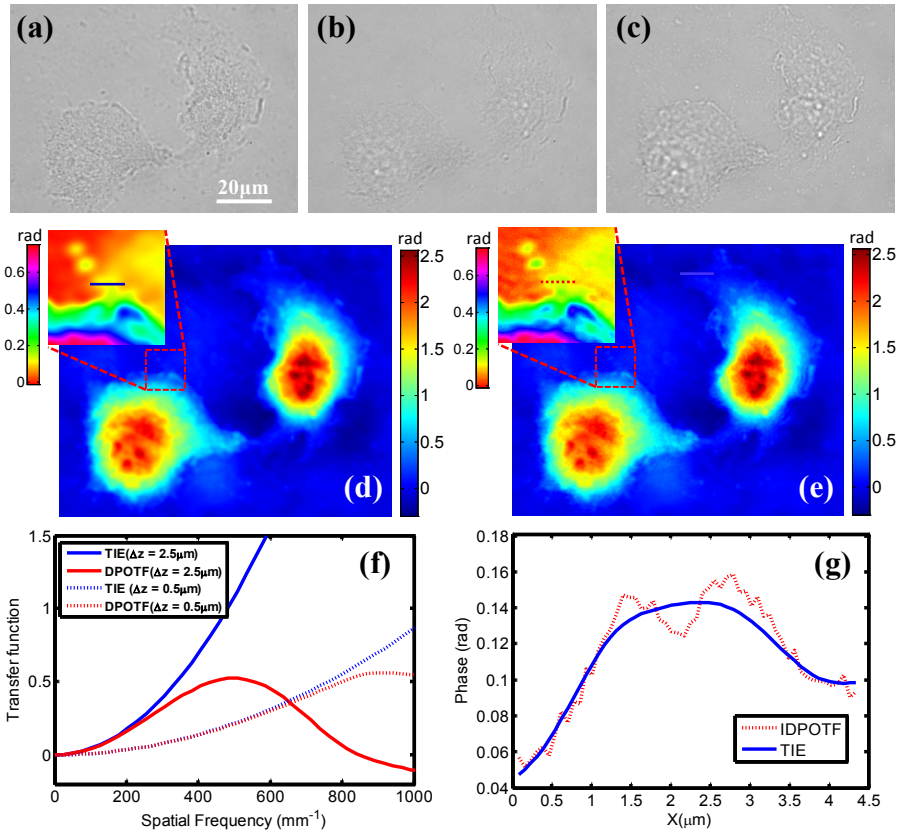

Fig. 6. Experiment validation of IDPOTF method. (a-c) Intensity images with defocus distance –2.5, 0, 2.5 μm (d) Phase map recovered by traditional TIE. (e) Phase map recovered by IDPOTF. The insets show the magnified areas corresponding to boxed regions. (f) TIE phase CTF and DPOTF for defocus distance 2.5, and 0.5 μm . (g) The intensity distributions along the blue solid line and the red dotted line shown in (d) and (e).

#193903 - $15.00 USD Received 15 Jul 2013; revised 16 Sep 2013; accepted 17 Sep 2013; published 1 Oct 2013
(C) 2013 OSA

To demonstrate the dynamic phase imaging ability of TL-TIE, a single cell was studied with time-lapse imaging and three snapshots from the video sequence corresponding to object planes at –2.5, 0.0 and + 2.5 μm are shown in Figs. 7(a)–7(c), respectively. The quantitative phase recovered using the IDPOTF method is shown in Fig. 7(d). We also presented the sequential reconstruction movie (Media 2), replayed at a much higher frame rate. Once quantitative phase information is obtained, other types of microscopy such as DIC, phase contrast, and dark field can be numerically simulated. Figure 7(e) shows the corresponding simulated DIC microscopy image by digitally calculating the phase gradient in the direction of the image shear (45°), which produces a shadow-cast image that effectively enhance the gradient of optical paths for both low and high spatial frequency details present in the specimen (Media 2). By using the quantitative phase information obtained, the physical thickness of cell can be obtained. Figure 3(f) shows the pseudo-color 3D rendering of the specimen, which shows high quality and high contrast surface details on the cell and provides an accurate profile of optical thickness. Note the refractive index of the medium is measured to be 1.341 with a refractometer, and the refractive index of MCF-7 is assumed to be 1.360 [38] for the entire cell contents for simplicity. The time series (Media 3) provides complete four-dimensional information of the cell's 3D spatial images as well as the time evolution of those images. It is clear to see the movement of very tiny subcellular details, i.e. the nucleus in the cell center, ruffles on the membrane, and the lamellipodia in the cell periphery. Besides, since our method use partially coherent white light and the continuous phase map can be directly recovered without phase unwrapping, the results are not plagued with problems of speckle noise and phase unwrapping errors. Note some low-frequency fluctuations on the background are perceivable, which is due to the greater sensitivity to noise at low spatial frequencies [as we can see in Fig. 6(e), the value of transfer function approaches to zeros as the frequency goes to zero, which is the common problem in the TIE-based methods]. Of course, some other factors such as evaporation or instability of the cell-culture medium may also contribute to the problem.

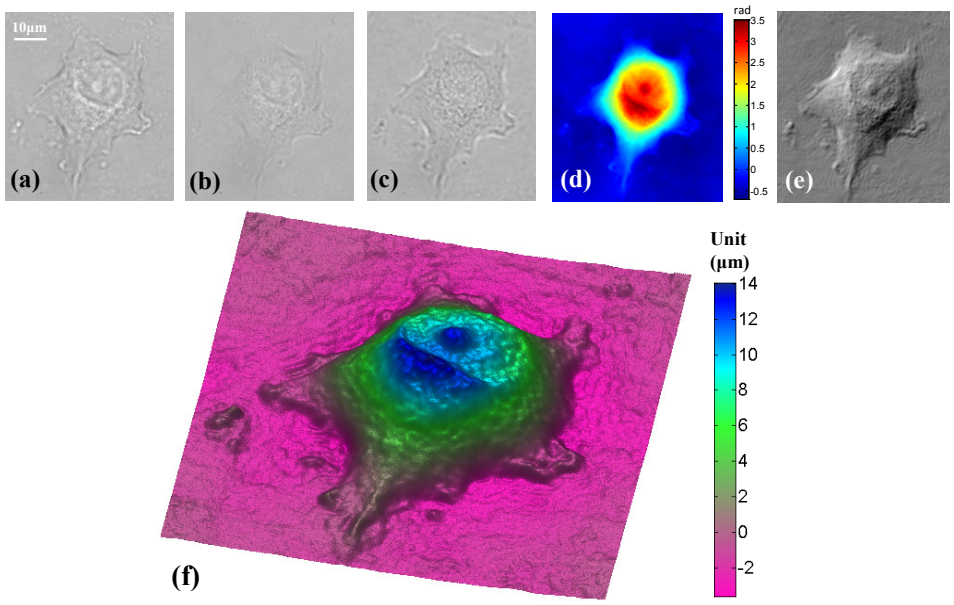

Fig. 7. Time-lapse quantitative phase imaging of an individual MCF-7 using TL-TIE. (a-c) Intensity images with defocus distance –2.5, 0, 2.5 μm (d) Phase map recovered through IDPOTF (Media 2). (e) Digitally simulated DIC image from (d) (Media 2). (f) 3D pseudo-color rendering of the cell thickness (Media 3).

#193903 - $15.00 USD Received 15 Jul 2013; revised 16 Sep 2013; accepted 17 Sep 2013; published 1 Oct 2013
(C) 2013 OSA

5. Conclusions

In summary, a new quantitative phase microscopy system, TL-TIE, has been demonstrated by introducing the ETL as a fast axial scanning device to realize the non-mechanical focusing control for high-speed TIE phase imaging. The flexibility offered by the TL-TIE system allows for the rapid recording of intensity images at different defocus distances with constant magnification, simple and straightforward implementation on conventional microscope at low cost without altering its original high imaging quality. Furthermore, TL-TIE combines these merits with other unique advantages inherits from the traditional TIE phase imaging, offering a simple, non-interferometric, high-speed, high-resolution, and unwrapping-free approach for quantitative phase microscopy.

The TL-TIE system has been successfully applied to measure the thickness of microlens array and showed that OFS accurately reproduced the expected thickness distribution, which is in good agreement with the DHM result and the value quoted by the manufacturer. We have proven and experimental demonstrated that the OFS method could be well applied for relative strong phase object and extend the validity of TIE beyond the limit of small distances by using more axial intensity images. It has been also shown that the OFS method could provide accurate phase image even under severely noisy conditions.

As another contribution of this work, we have introduced IDPOTF to remove the phase blurring related to the defocusing and illumination coherence, thus improve the spatial resolution of TIE phase imaging with only three intensity images. The result of live cell imaging demonstrate that the proposed TL-TIE is a competitive and promising tool for investigations of dynamic cellular processes, like cell migration, effects of drug effectiveness, and toxicity assessment of bio-functionalized nano-materials on living cellular systems.

Appendix A:

Consider a complex object field $u_0(x,y) = A_0(x,y)\exp[i\varphi(x,y)]$, where $A_0(x,y)$ is amplitude modulation of the object which equals to $\sqrt{I_0(x,y)}$, $\varphi(x,y)$ is phase. To make the formulae more compact, we denote the lateral dimensions (x,y) as $\mathbf{r}$; and its corresponding Fourier conjugates are given by $\mathbf{u}$. Assuming a slowly-varying object, i.e., $\left|\varphi(\mathbf{r})-\varphi(\mathbf{r}-\lambda z\mathbf{u})\right| \ll 1$, and $A(\mathbf{r}-\lambda z\mathbf{u}) \approx A(\mathbf{r}) - \lambda z\mathbf{u}\nabla A(\mathbf{r})$, where z is the defocus distance from the focus plane, the Fourier transform of the intensity image captured at distance z can be represented by [39]:

$$\begin{aligned}\hat{I}_z(\mathbf{u}) &= \hat{I}_0(\mathbf{u}) + 2\left[\sin(\pi\lambda z u^2) - \pi\lambda z u^2\cos(\pi\lambda z u^2)\right]\mathcal{F}\left\{I_0(\mathbf{r})\varphi(\mathbf{r})\right\} \\ &-\cos(\pi\lambda z u^2)\frac{\lambda z}{2\pi}\mathcal{F}\left\{\nabla\left[I_0(\mathbf{r})\nabla\varphi(\mathbf{r})\right]\right\}.\end{aligned} \tag{15}$$

Note here $u^2 = |\mathbf{u}|^2$. The Fourier transform of intensity derivative estimated by a fixed-degree SGDF with $2n+1$ intensity measurements equally separated by Δz is

$$\begin{aligned}&\mathcal{F}\left\{\frac{\partial I(\mathbf{r})}{\partial z}\right\} \approx \frac{\sum_{j=-n}^{n} a_j \hat{I}_{j\Delta z}(\mathbf{u})}{\Delta z} \\ &= \frac{1}{\Delta z}\sum_{j=-n}^{n} a_j \hat{I}_0(\mathbf{u}) \\ &+ \frac{1}{\Delta z}\sum_{j=-n}^{n} a_j\left[\sin(\pi\lambda j\Delta z u^2) - \pi\lambda j\Delta z u^2\cos(\pi\lambda j\Delta z u^2)\right]\mathcal{F}\left\{I_0(\mathbf{r})\varphi(\mathbf{r})\right\} \\ &- \frac{\lambda}{2\pi}\sum_{j=-n}^{n} a_j j\cos(\pi\lambda j\Delta z u^2)\mathcal{F}\left\{\nabla\left[I_0(\mathbf{r})\nabla\varphi(\mathbf{r})\right]\right\}.\end{aligned} \tag{16}$$

#193903 - $15.00 USD Received 15 Jul 2013; revised 16 Sep 2013; accepted 17 Sep 2013; published 1 Oct 2013
(C) 2013 OSA

Since the coefficients of SGDF $\{a_j | -n \le j \le n\}$ are odd-symmetric with the central weight always null [17, 40], the first term on RHS of Eq. (16) reduces to zero. Obviously, to ensure that the SGDF can produce unbiased phase estimates by using TIE, $\mathcal{F}\{\partial I(\mathbf{r})/\partial z\}$ should approximate $-(\lambda/2\pi)\mathcal{F}\{\nabla[I(\mathbf{r})\nabla\varphi(\mathbf{r})]\}$, which further means the following two requirements should be satisfied:

$$\sum_{j=-n}^{n} a_j \left[\sin(\pi\lambda j\Delta z u^2) - \pi\lambda j\Delta z u^2 \cos(\pi\lambda j\Delta z u^2)\right] \to 0; \tag{17}$$

and

$$\sum_{j=-n}^{n} a_j j\cos(\pi\lambda j\Delta z u^2) \to 1. \tag{18}$$

The basic idea behind OFS is to extract the best frequency components of the phase images obtained from SGDFs with various degrees and then recombine them into a composite phase. The cutoff frequency for the complimentary filter bank is determined according to the congruity between the frequency response of the SGDF and the ideal derivative filter. Only when the phase component fall into the frequency range which satisfy $\sum_{j=-n}^{n} a_j \sin(\pi\lambda j\Delta z u^2) \approx \pi\lambda\Delta z u^2$, they can be considered as '*correct reconstruction*' or '*reliable retrieval*' [17]. It is not difficult to show that when $\sum_{j=-8}^{n} a_j \sin(\pi\lambda j\Delta z u^2) \to \pi\lambda j\Delta z u^2$, then $\sum_{j=-n}^{n} a_j j\cos(\pi\lambda j\Delta z u^2) \to 1$ with a precision of $O(\Delta z^3 u^6)$, therefore Eq. (18) can be satisfied. Then the first condition can be directly satisfied by taking Eq. (18) into Eq. (17). So finally we have

$$\mathcal{F}\left\{\frac{\partial I(\mathbf{r})}{\partial z}\right\} \approx -\frac{\lambda}{2\pi}\mathcal{F}\{\nabla[I(\mathbf{r})\nabla\varphi(\mathbf{r})]\}. \tag{19}$$

This reduces to the standard TIE formulation [Eq. (6)] in Fourier domain. It therefore demonstrates that the OFS method can successfully extend the TIE method beyond the small-defocus-limit and making only the assumption of slowly-varying object.

Acknowledgments

This project was supported by the Research Fund for the Doctoral Program of Ministry of Education of China (No. 20123219110016), Translational R&D and Innovation Fund (TIF) grant of the Singapore Ministry of Education (No. MOE2012-TIF-1-T-003), and the Research and Innovation Plan for Graduate Students of Jiangsu Higher Education Institutions, China (No. CXZZ11_0237). Chao Zuo gratefully acknowledges the financial support from China Scholarship Council (No. 201206840009).